

The development of zones of active plasticity during mode I steady-state crack growth in thin aluminum sheets



Syed Saad Javaid^{a,b}, Wade R. Lanning^a, Christopher L. Muhlstein^{a,1}

^a School of Materials Science and Engineering, Georgia Institute of Technology, Atlanta, GA, USA

^b College of Aeronautical Engineering, National University of Sciences and Technology, Pakistan

ARTICLE INFO

Keywords:

Zones of active plasticity
Steady-state crack growth
Thin sheets
Ductile tearing
Fracture mechanics

ABSTRACT

Cracks grow in millimeter-scale, ductile metal sheets when a transverse neck fracture process zone fails by microvoid coalescence. Here we showed that the crack growth mechanism changed to a different steady-state process when sheet thicknesses were $\lesssim 100 \mu\text{m}$. We experimentally quantified the shape, extent, and evolution of the process zones in 1235 Al and showed that three zones were operating: A large, uncontained plastic zone (PZ) ahead of the crack tip had an embedded, steady-state zone of active plasticity (ZAP) that surrounded a transverse neck fracture process zone (FPZ) which failed via a microvoid-free shear mechanism.

1. Introduction

The study of plastic and fracture process zone extent and morphology is fundamental to understanding and predicting crack growth in materials. In ductile metals the characteristics of the plastic zones vary with thicknesses, texture and defect configurations near the crack tip [1–3]. The size of the plastic zones relative to the specimen dimensions can be used to determine which analysis methods can be used to quantify the fracture toughness of a material and the conditions for and stability of crack growth. Unfortunately, the distinction between small- and large-scale crack tip yielding conditions has led to considerable confusion in the literature about the practical limitations of using conventional fracture mechanics methods to describe crack growth in extremely thin, ductile materials such as the commercially pure aluminum used in this study. In this paper we clarify the crack growth mechanisms and fracture mechanics methods for extremely thin, ductile sheets and report the size and evolution of the associated crack tip process zones.

Linear Elastic Fracture Mechanics (LEFM) and Elastic Plastic Fracture Mechanics (EPFM) approaches (with the crack tip parameters K or J , respectively) are most effective when the crack tip plastic zones are *contained* in a small region (compared to the rest of the specimen) with a boundary that can be described with a singular stress field (Fig. 1) [4–7]. In the case of K , the crack tip plastic zone must relatively small so that the singular, linear elastic stress field can be used to describe crack growth (i.e., small-scale yielding conditions are found at the crack tip). When the crack tip plastic zone is not small enough, alternative approaches must be used to describe crack growth under these large-scale yielding conditions. Because of its energetic basis, the path independent J -integral is a robust concept that can be applied to small and large-scale yielding conditions *even when a convenient crack tip parameter is not available*[8,9]. However, it is important to clarify the sizes and types plastic zones where it can be applied effectively as a crack tip parameter. While it is relatively straightforward to calculate the J -integral using finite element methods, experimentally verified J -controlled crack growth conditions are most often found when the extent of plasticity is *contained* in a small region (albeit larger than

E-mail address: christopher.muhlstein@mse.gatech.edu (C.L. Muhlstein).

¹ School of Materials Science and Engineering, Georgia Institute of Technology, 771 Ferst Dr NW, Atlanta, GA 30332, USA.

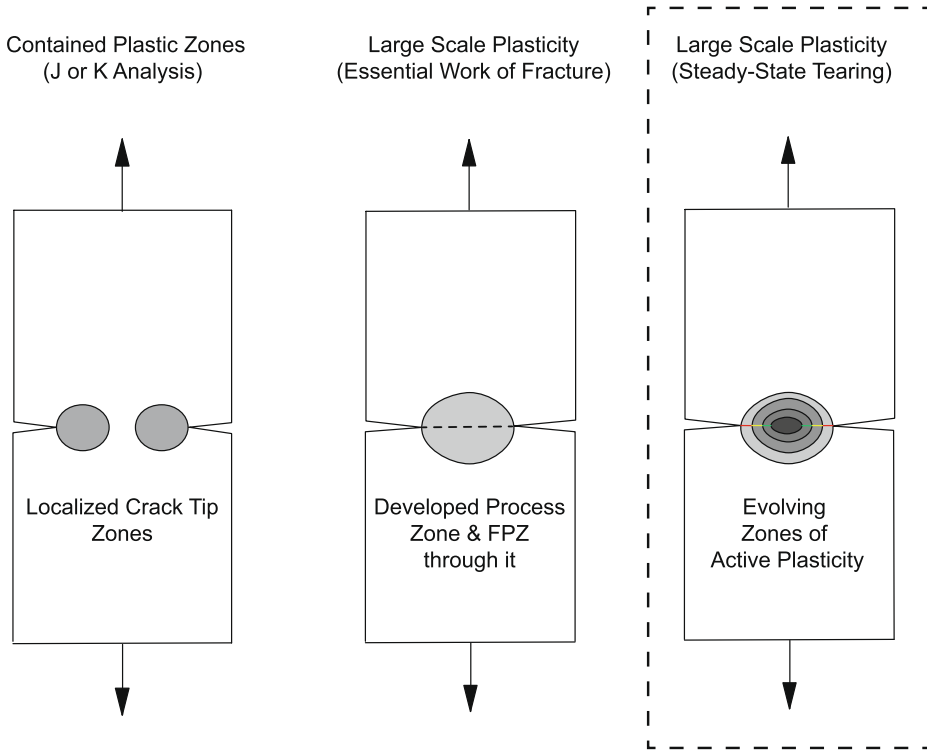


Fig. 1. Schematic of the process zones in double edge notched tensile (DENT) specimens and their relationships to various analysis methods. The plastic zones must be contained in a small, well-defined region for linear elastic (K) or elastic plastic (J) analysis methods to be applicable. When the plastic zone is large (relative to the uncracked ligament) the essential work of fracture method is used. During tearing of ductile thin sheets, the tearing mechanism has three stages and steady-state zones develop.

the plastic zones associated with small-scale yielding conditions) that can be defined by singular field (e.g., the Hutchinson, Rice, and Rosengren (HRR) singularity [8,10–12]). It is important to note that while these conditions are generally called “large scale yielding”, the plastic deformation of interest is still contained in a small zone (relative to the dimensions of the specimen and uncracked ligament) ahead of the crack tip. Furthermore, the fracture process zone is embedded within this well-defined elastic-plastic zone [5]. The plastic zone in materials that undergo extensive, large scale plasticity cannot be described by convenient, contained singular fields [13]. It is extraordinarily difficult to validate J -controlled crack growth under these conditions, especially when the material form is very thin. References [14,15] are a couple of the many examples of how the practical (as opposed to fundamental) limitations of J -controlled growth were established. An alternative strategy to address uncontained plastic zones is to force predictable plastic zone scaling with experiment designs such as Double Edge Notch Tensile (DENT) specimens and the essential work of fracture (EWF) method [4,16–24] (Fig. 1). The EWF technique leverages the 2-stage fracture mechanism of millimeter-scale ductile sheets where the crack growth process begins with the formation of a well-defined plastic zone and transverse neck across the full width of the sheet. Then a narrow, embedded fracture process zone develops ahead of the crack tip as the crack grows [21,24]. The EWF analysis assumes that once the ligament has yielded and neck formed, all subsequent energy added to the system is used to develop the Fracture Process Zone (FPZ). The essential fracture energy is used to create a fracture surface across the neck via a void nucleation, growth, and coalescence process [18,22,25]. When applicable, the EWF method relies on a contained, elliptical plastic zone scaling that can also be evaluated as a special case of the more general J -integral [9,24].

The utility of the EWF method and its relationship to the elastic-plastic crack tip parameter, J_{lc} , requires suitable combinations of materials properties (i.e., yield and hardening) and sample geometry (particularly thickness and remaining ligament size) [26]. Pardoen et al. clearly note in Section 6 of [22] that the EWF method is not applicable to very thin, ductile sheets where void formation and coalescence is limited. We showed in our previous work that tearing of very thin (sub 1 mm) ductile sheets cannot be characterized using LEFM or EPFM because the crack tip process zones are extremely large and are not contained in conventional crack tip fields [13,27]. These studies also established that ductile tearing in thin (sub-mm) sheets progresses through three stages (Fig. 2): an initiation stage (I) that is followed by a transition (II) to steady-state crack growth (III). A critical difference between very thin (sub-millimeter) and thicker sheets is that the third stage is characterized by the steady-state crack growth resistance parameter, σ_c , which scales with the net (remaining) section.² Conventional approaches (including the EWF) describe thin sheet tearing as a two-

² Steady-state crack growth is achieved when a crack propagates through (effectively) invariant damage zones which allow balancing of driving force and crack growth resistance.

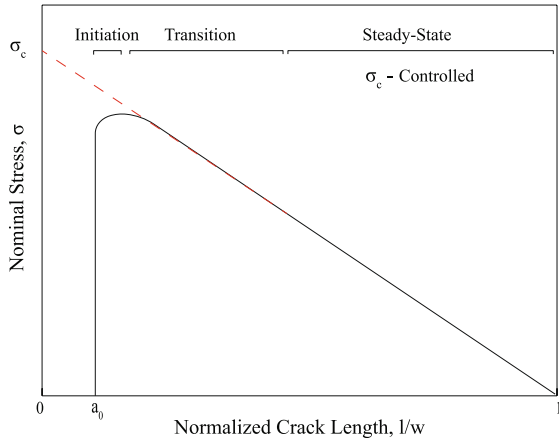


Fig. 2. Schematic of the three stages of ductile tearing and steady-state crack growth showing initiation (I), transition (II) and steady-state crack growth (III). The nominal stress, σ , as a function of normalized crack length becomes linear once steady-state conditions are reached.

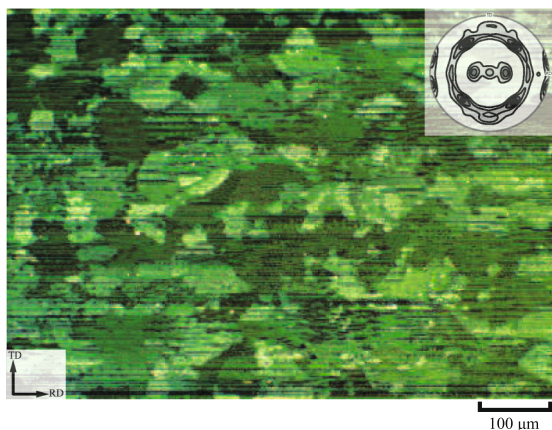


Fig. 3. Polarized light optical image of the grain morphology of the anodized 25.4 μm 1235 aluminum (lineal intercept grain size 127 μm). The horizontal streaks in the image were from the surface roughness of the as-rolled sheet (RD and TD were the rolling and transverse directions, respectively). The inset pole figure indicates cubic (100)[001] texture.

stage damage mechanism [5,28] where large-scale plasticity and transverse necking occur prior to fracture via a microvoid coalescence mechanism. First a plastic zone (PZ) forms, then the fracture process zone (FPZ) drives the crack through the established PZ without altering it substantially [16,17,27]. Here, we experimentally measure the extent and evolution of process zones during tearing of very thin (sub-millimeter), ductile commercially pure Al sheets to establish a different crack growth mechanism and validate a steady-state crack growth analysis method.

2. Materials and methods

Specimens were made from 25.4 μm thick commercially pure 1235 aluminum foil stock and cut into dogbone-type specimens based on the ASTM E345 A geometry [29]. The specimens had the same nominal reduced section length (30 mm), reduced section width (12.5 mm), gauge length (20 mm) and fillet radius (9.5 mm) ([Supplemental Fig. 2](#)). The samples were cut using a Sizzix eClips2 blade cutter, and notches were cut using QuikLaze-50ST2 machining laser or manually using a razor blade. The same 25.4 μm material stock and specimen dimensions were used in our earlier studies and extensive material characterization was performed [13,27]. The material has an in-plane lineal intercept grain size of 127 μm and a cubic (100)[001] texture through the thickness ([Fig. 3](#)). A summary of tensile properties³ is included in [Table 1](#).

³ As we noted in [27], Elastic moduli much lower than the expected bulk, polycrystalline aggregate (or texture corrected) values [30] are routinely found in very thin sheets, foils, and films [31–39]. Originally discussed by Mott [40] and Friedel [41], “low” elastic moduli are a primarily a byproduct of elastic (bowing) of pinned dislocations. A summary of the modern literature on these interactions is detailed in Section 4.3 of the handbook by Blanter et al. [42].

Table 1

Uniaxial tensile properties of 25.4 μm 1235 aluminum sheets from DICT analysis. Yield stress σ_y and yield strain ϵ_y were computed with the 0.2% offset method [13,27].

Elastic modulus E (GPa)	Yield strength σ_y (MPa)	Yield strain ϵ_y	In-plane contraction ratio η_w	UTS σ_{uts} (MPa)	Converged σ_c MPa
23	27	0.0032	0.32	53	60

The dogbone-type specimens were modified to create double Edge Notch Tensile (DENT) specimens with edge notches of 1 mm; 2 mm; 3 mm; 4 mm; 5 mm (remaining ligament lengths 10.5 mm; 8.5 mm; 6.5 mm; 4.5 mm; 2.5 mm). 5 samples of each configuration (2 with laser cut notches, 3 with manual razor blade notches) were tested, for a total of 25 tearing experiments. See [13] for a detailed discussion about the independence of steady-state crack growth from precracking and notching method. All specimens were placed onto paper support backings before being fixed in the load frame grips to prevent wrinkling and misalignment as they were placed in the test frame grips. The specimens' grip sections were glued to the paper backing, while the fillets and reduced section were laid flat against the paper but were not glued. The specimens were then placed in the load frame's wedge grips. Once the specimens were secured in the grips, the portion of the paper backing behind the reduced section was removed. The specimens were lightly speckled using an Iwata airbrush and black acrylic paint to generate contrast for tracking. Previously published experiments established that the speckle pattern does not impact the results of tearing or tensile tests of the very thin aluminum sheets [13,27].

All specimens were tested in tension using an Instron 5848 mechanical test frame with wedge grips, 100 N Instron 2530-427 static load cell, and a magnetic linear encoder with 20 nm resolution (Heidenhain, Schaumburg, IL). The high resolution, low force testing system was mechanically isolated with a Minus-K BM-1 platform (Minus K Technology, Inglewood, CA USA) that is surrounded by a box enclosure. Please note that this is a high precision, low force, closed loop load frame that does not have the backlash and other control issues that are often associated with using high capacity load frames at low loads. Full field images of the specimens, including the grips, were used to directly measure rigid body motion and to verify precise specimen alignment for each test. Experiments were controlled by a custom-built program written in NI Labview 7.1 using a GPIB interface to control the load frame and record force and displacement data. Tests were performed in displacement control with crosshead displacement rates of 0.01 mm s^{-1} and 0.025 mm s^{-1} (initial strain rates of 0.02 mm/mm min^{-1} and 0.05 mm/mm. min^{-1}). These rates are slow enough to establish quasi-static condition. The data do not show sensitivity to these rates, and the creep rates reported for commercially pure aluminum at room temperature are much lower. The slower rate tests were used to capture high resolution strain maps using digital image correlation (DIC) as detailed below, while the faster rate helped to establish the steady state analysis and convergence dataset.

A 24 megapixel (6000×4000) Nikon D3300 DSLR camera fitted with a Nikon macro lens was used to capture full field (i.e., the full specimen gage section) images (line width resolution per MIL-STD-150A better than 40 μm) before and during experiments. The specimens were illuminated with a 50.8 mm Dolan-Jenner FLD light diffuser connected to a Dolan-Jenner Fiber-Lite light source, and the camera was positioned such that it viewed the specimens *through* the light diffuser. A second fiber optic light source was placed behind the specimens to improve contrast. Thus, images were captured with an illumination condition analogous to combined bright field reflected and transmitted light microscopy. The camera settings were ISO 200, aperture f/8, and shutter 1/320 s. The camera was triggered using an Arduino Mega microcontroller with custom firmware which triggered the camera at a rate of 1 Hz using a connector wired from the Arduino to the camera's accessory port. The camera trigger microcontroller was synchronized to the experiment start with a TTL signal wired directly to the camera from the Instron load frame controller. The camera trigger microcontroller communicated the number and timing of its camera trigger signals with a computer through a USB serial connection, ensuring that force, displacement, and image capture data were synchronized to within 1 μs . The images captured during the experiments were used to measure the crack length with a spatial resolution of better than 0.6% (6 μm on a minimum length of 1 mm). The experiments were stopped when the cracks either reached the far edge of the specimens or a secondary crack initiated from the back edge. Representative fracture surfaces and fracture profiles were imaged using a Hitachi TM3030 bench-top scanning electron microscope (SEM) in "COMPO" backscatter imaging mode.

Three parameters were extracted from the nominal stress as a function of normalized crack length determined in the tearing experiments: the nominal stress and normalized crack length at initiation, σ_i and $\frac{l}{w_i}$; the onset of steady-state tearing, σ_{ss} and $\frac{l}{w_{ss}}$; and the steady-state tearing resistance, σ_c . The initiation of tearing was defined by the maximum force, P_i , that was measured during the experiment (consistent with the no-longer used ASTM B871-01) [13,43]. In the event of a plateau in the initiation region, the P_i with the smallest $\frac{l}{w}$ was identified as the initiation point. The traditional symbol for crack length, a , was not used because the definition of crack length was slightly different from in traditional fracture mechanics analyses [13,27]. As detailed in our previous publications [13,27], the onset of steady-state tearing and the steady-state propagation resistance, σ_c , was determined using an analysis of variance (ANOVA) method using the open source Anaconda Python 2.7 (64-bit) as detailed in Appendix A.

The specific work of fracture was determined from the force–load line displacement curves using a method similar to that detailed in [23,24]. We determined the essential work of fracture (EWF) by calculating specific cumulative work done in advancing the crack as a function of the remaining ligament size measured from the optical images. Specifically, the measured force and crosshead displacement were used to calculate the specific incremental work, and the total (normalized by remaining ligament area) was calculated by using Euler's method to numerically integrate for each of the 5 experiments per condition. The EWF was then extracted from the ordinate intercept of a linear fit of the mean specific cumulative work as a function of initial remaining ligament length using least squares method (R^2 value of 0.99) in OriginLabs OriginPro2017 software package.

We experimentally measured the spatial distribution of strains from the full field optical images using our in-house developed, open source platform digital image correlation (DIC) code that we have used in our previous research. A regular grid of approximately 10,000 points was defined in the first image and then tracked through the image sequence using a Python (Anaconda 2.7) implementation of the OpenCV sparse optical flow feature tracking algorithm calcOpticalFlowPyrLK. The points were tracked between the reference image X and the current image x . Any features that the algorithm failed to find or could not be tracked back to within 2 pixels of their location in the previous image in the sequence were discarded. A least squares fit of the raw displacement data points was used to find the local gradient. A local area fit radius of $2\times$ feature spacing was used with 10,000 points in the selected tracking area. We then used Voronoi triangulation to interpolate the strains and plotted them using matplotlib Python package. The algorithm was validated by using synthetic images (of similar pixel densities) with known strain fields and tracking points on the grid. The sub-pixel tracking accuracy for a given specimen was validated prior to each experiment by using a 3-Axis Rigid Body Motion (RBM) calibration by translating the camera on a precisely aligned on eTrack XYZ (Newmark Systems, Rancho Santa Margarita, CA, USA) three axis stage while capturing images of the stationary test specimen at fixed motion intervals ([Supplemental Fig. 1](#)).

Direct strain measurement techniques like digital image correlation not only allowed us to capture accumulated strains - but also provided an opportunity to quantify strain evolution with respect to any reference frame. Conventional analyses use a constant reference frame corresponding to the undeformed specimen in the beginning of the experiment ($X = \text{Image } 0$). By selecting specific testing windows and analyzing evolving strains in conjunction with accumulated strains, we also quantified the regions of evolving strains. Strain maps were used with different reference X frames to highlight specific areas of interest. This allows us to capture the rate at which strain evolves and examine interactions between developing plastic zones: how they merge and their extents during evolution. The moving window, or evolving strain rate, methodology was used with multiple intervals to capture the sensitivity of the interval size and determine a suitable window that was utilized for subsequent analysis. The axial strain, ϵ_{yy} , was thresholded used by using a 1:1 pixel mapping to the starting crack length and evaluated a strain line profile at $X = \frac{w-l}{2}$, the mid point between the crack tips of the reference image. We determined the maximum strain value and thresholded the strain map such that strains above that level were characterized as the FPZ. A sensitivity analysis for various thresholding levels was used and one was selected based on capturing maximum strain distribution and limiting noise. The same thresholding level was used for subsequent analysis to determine the shape and extent of the deformation zones. The effect of thresholding on the zone extent is detailed in the following Results and Discussion section.

3. Results and discussion

Tearing of sub-millimeter, ductile metal sheets involves crack tip plasticity that is far larger in spatial extent than the contained plastic zones that are typically evaluated with conventional linear elastic and elastic plastic engineering fracture mechanics methods. The gross plastic deformation is readily seen in optical images of growing cracks ([Fig. 4](#) and [Supplemental Movie 1](#)) in our 1235 Al, 24.4 μm thick sheets. The contrast in the optical images is from deformation bands that formed when multiple slip bands emerged at the free surfaces (a commonly observed feature in FCC metals). We have noted in our previous studies of 25.4 μm ; 50.8 μm ; 125 μm 1235 Al sheet (using single edge and middle notched tension specimens) that the crack tip plastic zones are uncontained and span the remaining ligament when steady-state conditions are achieved. The size and shape of the plastic zone cannot be predicted with established, singular crack tip stress fields (i.e., the linear elastic and HRR-type elastic-plastic fields) because of some important features of the tearing mechanism. Previously we noted that tearing in the single edge and middle notch tensile specimens progressed through a three stage process ([Fig. 2](#)). After an initiation phase, which terminates at the largest applied force, the net section stress necessary to continue crack growth decreases. Eventually steady-state conditions prevail, and a characteristic steady-state tearing



Fig. 4. Optical image of a crack that grew under steady-state conditions in a 25.4 μm thick double edge notched tension specimen. The extensive, uncontained plastic deformation in the ligament ahead of the cracks was clearly visible as lines oriented perpendicular to the loading (and rolling) direction.

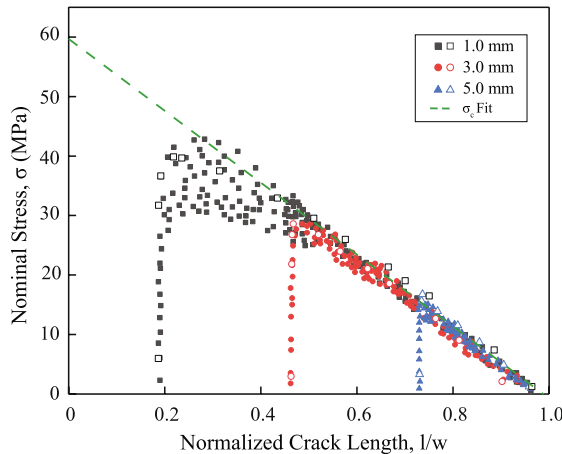


Fig. 5. Ductile tearing of 25.4 μm Double Edge Notch Tensile (DENT) specimens showing convergence to steady-state (σ_c -controlled growth) for double edge notch lengths of 1 mm; 3 mm; 5 mm. The slow rate tearing experiments used for DIC are indicated with colored open symbols, and are indistinguishable from the faster rate experiments. The one standard deviation error bars are smaller than the symbol representing the data points.

resistance can be defined. We previously showed that the average characteristic steady-state resistances measured with single-edge and middle-notch tensile specimens was $\sigma_c = 60 \pm 2.3$ MPa [27]. When the sheets are thicker than 1 mm and the yield strength is sufficiently high, the DENT specimen geometry forces the plastic zone to be contained in a well-defined (albeit large) region between the two notches so that the essential work of fracture (EWF) analysis method can be applied. In the current work we established the unique deformation and crack growth mechanisms of quasistatic, steady-state tearing in very thin, ductile sheets by quantifying the extent and evolution of the crack tip process zones.

Consistent with our previously established similitude conditions in SENT and MT specimens, the steady-state tearing behavior of the 25.4 μm thick Al (Figs. 5 and 6 and Table 2), DENT specimens also exhibited a three stage process where steady-state growth conditions prevailed. Initiation of the tearing process from the laser and blade cut notches were indistinguishable from one another, and the transition to steady-state behavior required very little crack extension. The crack growth behavior at conventional and slower strain rates (for enhanced DIC resolution) were indistinguishable (Figs. 5 and 6). Moreover, the characteristic steady-state tearing resistance of 59 MPa for the 25 specimens in the present study was essentially the same as what we measured for the same material using SENT and MT specimens [13,27]. The subset of slower strain rate experiments had a characteristic steady-state tearing resistance of $\sigma_c = 57$ MPa. Like the previously studied SENT and MT specimens, the fracture and free surface images of the DENT showed that the crack path was transgranular. The fracture of the DENT specimens occurred by the formation of a transverse (through thickness) neck with nearly 100% reduction in area (i.e., final separation occurred along a fine "knife edge") that was essentially free of voids (Fig. 7). The transition from the notch to the transverse neck appeared as an obtuse triangular region with two vertices located at the free surfaces of the foil, and one vertex along the midline of the sheet (i.e., the length of the transition region is on the order of the sheet thickness). This transition geometry differs from those found in higher yield strength, thin sheet

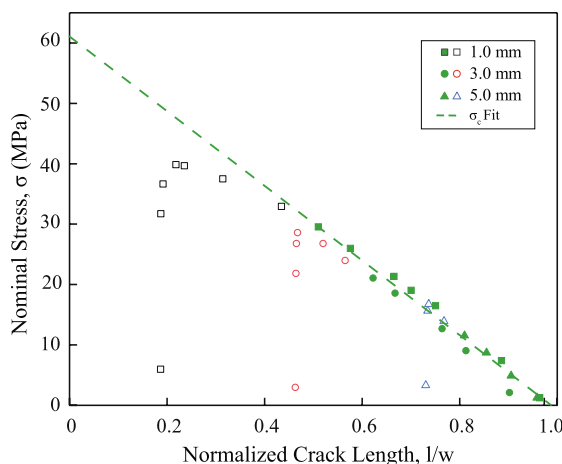


Fig. 6. Ductile tearing analysis of 25.4 μm Double Edge Notch Tensile (DENT) specimens with slow rate (0.01 mms^{-1}) experiments used for DIC tracking. Solid symbols indicate the convergence regime determined by ANOVA [27] and used to determine σ_c for the slow rate experiments. The one standard deviation error bars are smaller than the symbol representing the data points.

Table 2

Mean nominal stress σ and corresponding mean $\frac{l}{w}$ values (with standard deviations shown as \pm) for initiation and steady state regimes for starting notch lengths of 1 mm; 3 mm; 5 mm.

Initial Notch	Initiation		Steady State	
	σ_{init} (MPa)	$\left(\frac{l}{w}\right)_{init}$	σ_{ss} (MPa)	$\left(\frac{l}{w}\right)_{ss}$
1 mm	37.04 \pm 4.46	0.27 \pm 0.01	26.55 \pm 1.04	0.55 \pm 0.01
3 mm	27.28 \pm 1.01	0.49 \pm 0.01	17.85 \pm 0.79	0.68 \pm 0.01
5 mm	13.96 \pm 1.44	0.74 \pm 0.01	9.12 \pm 0.53	0.82 \pm 0.01

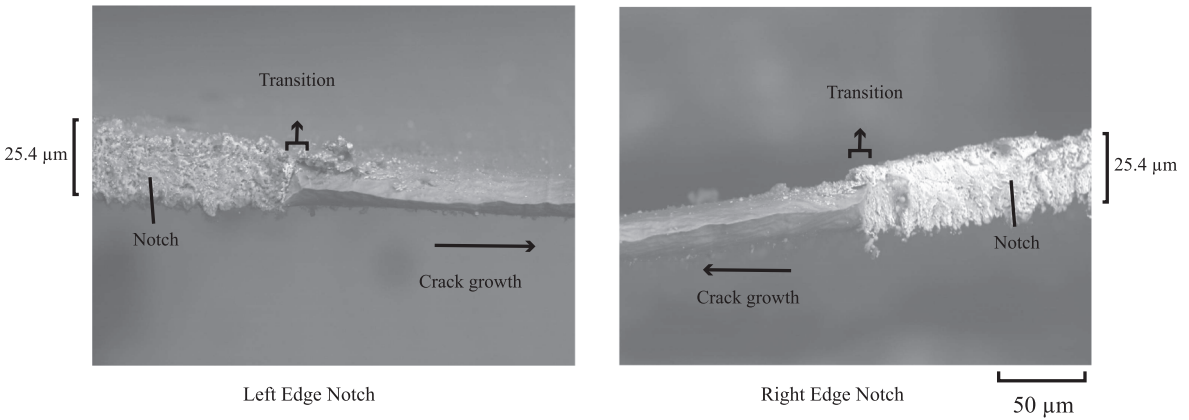


Fig. 7. Fracture surface profile illustrating crack initiation, transition and propagation via through thickness necking in a representative DENT 1 mm sample. The final separation occurred along a "knife edge" that was essentially free of voids.

materials in that the flat, dimple void rupture fracture surface is vanishingly small [22,23].

A key feature of the EWF analysis method of the DENT is that a self-similar, circular or elliptical plastic zone forms between the notch (crack) tips, and the remaining energy is used for crack extension in the fracture process zone (FPZ) [21–23]. The ordinate intercept of a plot of specific work dissipated in the specimen as a function of notch size is then the essential work of fracture. When we applied this analysis method to our 25.4 μm thick commercially pure aluminum (Fig. 8), the essential work of fracture was a non-physical (negative) energy of -1.5 MJ m^{-2} . Pardo et al. [22] noted that the EWF method was not applicable to very thin ($\leq 100 \mu\text{m}$), very ductile sheets (pure Pb in their case) because the underlying fracture mechanism was presumably different, but how has not been appreciated until our current work. The EWF testing and analysis method is effective when the scaling and damage partitioning in the DENT specimen provides contained plastic and damage zones. Like Pardo et al.'s thin Pb sheets, optical and scanning

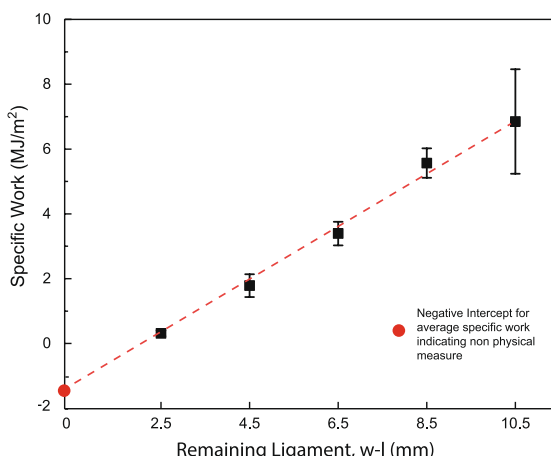


Fig. 8. Essential work of fracture analysis for 1 mm; 2 mm; 3 mm; 4 mm; 5 mm DENT samples. The negative essential work of fracture is a byproduct of the unique, steady-state tearing mechanism. Error bars indicate the standard deviation of the measurements, and those not shown were within the symbol representing the data points.

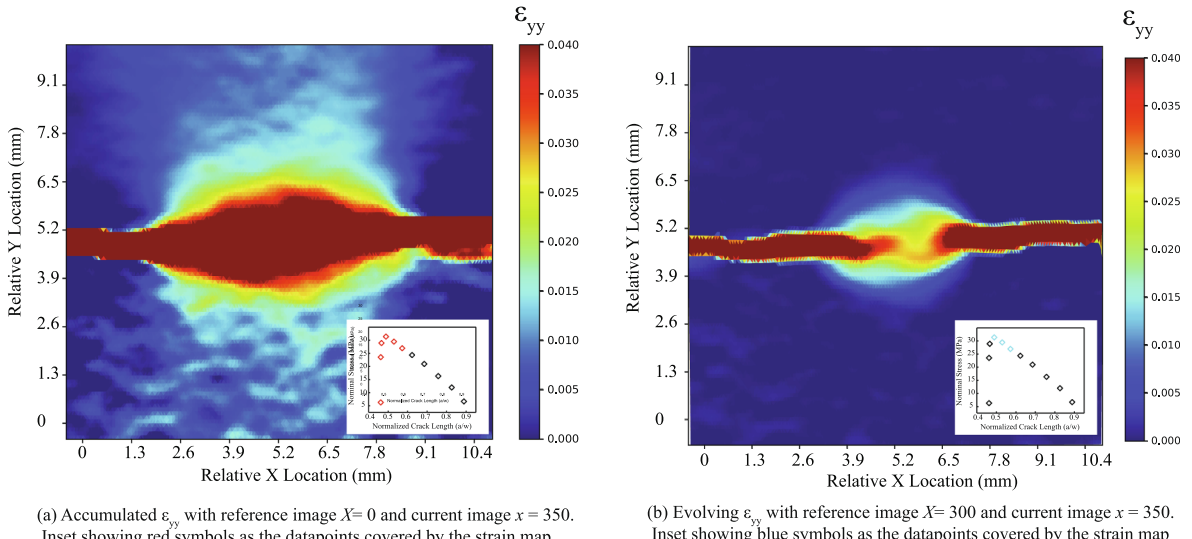


Fig. 9. ϵ_{yy} Strain maps of a 3 mm DENT specimen illustrating the difference between accumulated strains and the incremental (evolving) strains. Inset of the associated three stage tearing process indicates the intervals used for the strain maps (red datapoints captured for accumulated strain maps, while light blue datapoints indicating the interval used for the evolving strain map). Error bars not shown were within the symbol representing the data points. (For interpretation of the references to colour in this figure legend, the reader is referred to the web version of this article.)

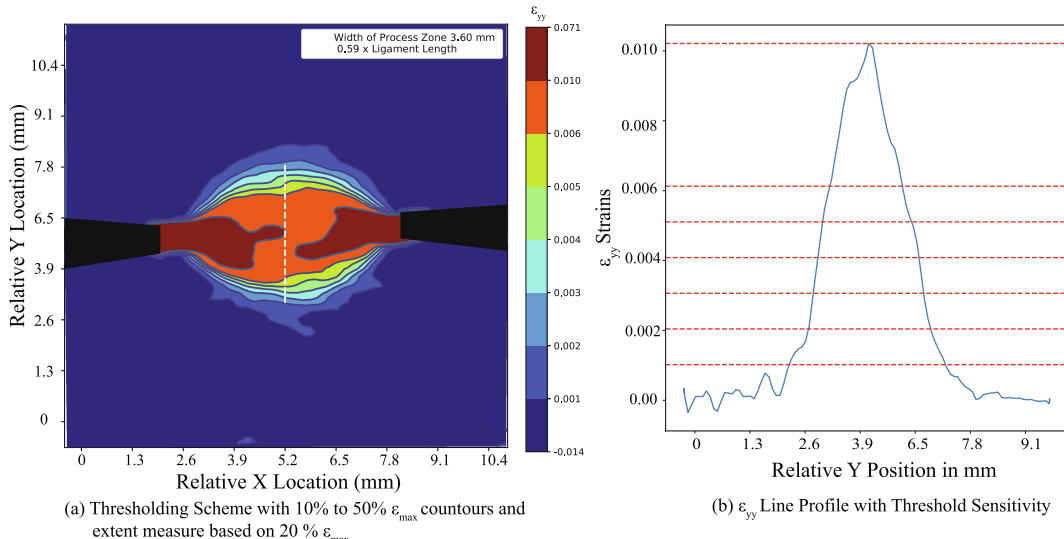


Fig. 10. Thresholding Scheme ϵ_{yy} used for the strain maps in a representative 3 mm DENT Specimen. A strain line profile at the mid point between the crack tips ($X = \frac{w-l}{2}$) was used to determine the maximum strain ϵ_{max} and fractions (10% to 50%) of ϵ_{max} were explored to quantify zones.

electron images of the crack paths and fracture surfaces of our 1235 Al sheets showed that plastic deformation extended completely across the uncracked ligament and that the mechanism was an essentially pure shear, transverse necking mechanism with virtually no void formation. Our direct measurements of the crack tip process zones revealed that the very thin sheet tearing mechanism was quite different from > 1 mm sheets, which explained the apparent limitations of the EWF method [21,22].

The requirements for the essential work of fracture method are that the plastic zone between the notches must have a self similar (circular or elliptical) shape that develops rapidly during initiation, and the zone remains invariant as tearing proceeds.⁴ It was readily apparent that the underlying mechanisms of tearing in very thin, ductile sheets was different because the evolution and extent

⁴ It is important to note that this zone invariance was termed “steady-state” in some publications. The presence of a static, transverse necked zone across the width of the specimen is radically different from the steady-state cracking process described in our current work.

Table 3

Plastic zone extents using different thresholding levels.

Scaling	10% ϵ_{max}	20% ϵ_{max}	30% ϵ_{max}	40% ϵ_{max}	50% ϵ_{max}
PZ Extent	0.75	0.59	0.53	0.49	0.43

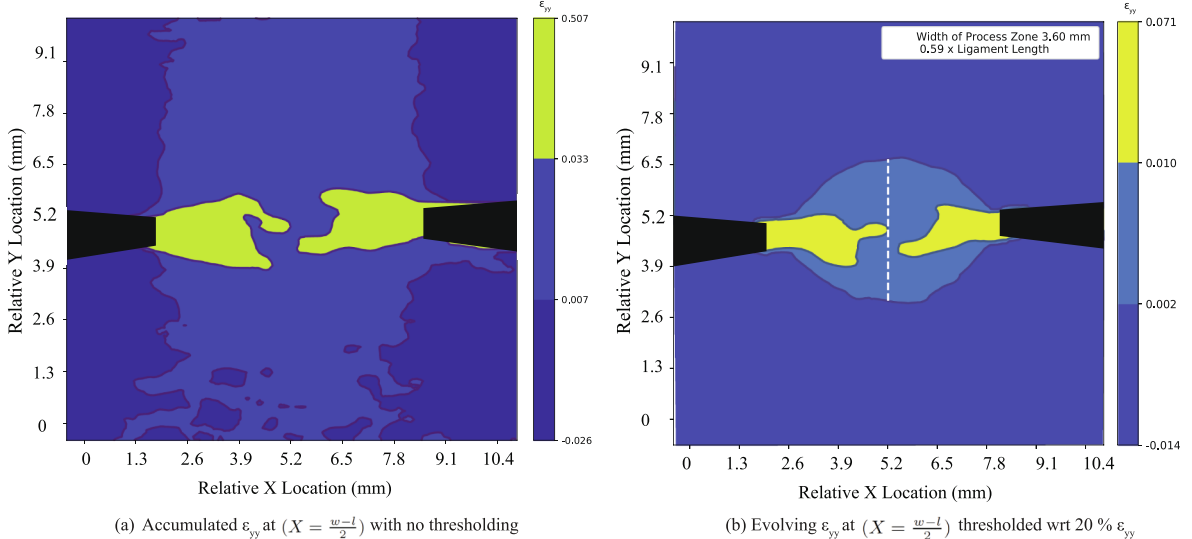


Fig. 11. Thresholded ϵ_{yy} Strain Map with FPZ characterized as strains above ϵ_{max} and PZ between 20% and ϵ_{max} . The PZ was 59% of the ligament length based on the starting crack tip locations as measured from the reference image.

of deformation and damage that were observed on the free surfaces of the specimens as the crack advanced (see Fig. 4 and supplemental movie A). We used these images of the tearing process to quantify the shape, extent, and evolution of the deformation and damage zones.

During the initiation stage of crack growth in our thin Al DENT specimens, large (well above the tensile yield strength) plastic strains developed (Fig. 9a). Since the ligament between the notch tips was fully-yielded before the crack advanced, the evolution of the crack tip process zones are obscured when the reference frame is the notched specimen at the start of the experiment (zero load). When we quantified the incremental strains during crack growth using a rolling window reference frame, we revealed the unique tearing mechanism of ultrathin sheets (Fig. 9b). Millimeter-scale sheets tear by the nucleation and growth of voids within a transverse neck that formed across the uncracked ligament during the initiation stage (i.e., before the crack grows) [21,22]. We found that the process zones were very different when the ductile sheets were much thinner and steady-state tearing developed. The extensive plastic zone between the crack tips (Fig. 9a) contained evolving, (light blue) elliptical zones of active plasticity (Fig. 9b). The (yellow and red) transverse neck fracture process zone was embedded within the zone of active plasticity. A schematic of the general features of the thin sheet tearing mechanism process zones are shown in Fig. 10.

We quantified the shape and extent of the process zones during the tearing experiments using a thresholding strategy (Fig. 10) along a strain line profile at the mid point between the crack tips ($X = \frac{w-l}{2}$). The maximum strain along the line was determined for a given experimentally measured strain map, and the extent set by thresholding to a predetermined fractions of ϵ_{max} . As shown in Fig. 10, we explored thresholding strains that ranged from 10% to 50% ϵ_{max} . The shape of the ZAP was consistent and elliptical, so we were able to identify a constant threshold level to define the zone size. As shown in Table 3, a threshold of 20% ϵ_{max} was chosen for all comparisons because it captured the extent of the ZAP strain distribution and ignored the small fluctuations in the adjacent plastic zone (Fig. 10). The threshold for the fracture process zone (yellow in Fig. 11) was ϵ_{max} , which corresponded roughly to the experimentally measured uniaxial tensile strain. Finally, the crack tip and mouth opening were identified in the optical images at the start and end of the incremental strain window, and were used to define the cracks (black masked regions). We then quantified how the ZAP and FPZ developed during the three stages of the ductile tearing crack growth process (Fig. 12).

Fig. 13 shows how the strains in the process zones evolved as tearing progressed from the 1, 3, and 5 mm long starting notches (shown as a row of strain maps in the figure). Thresholded, incremental strain maps before initiation, during the transition, and after steady-state were evaluated (shown as columns in the figure). Before initiation (defined by the maximum applied force in the tearing experiment) large strains develop and the ligament yields (i.e., strains are above the tensile yield strength), and the extent of the

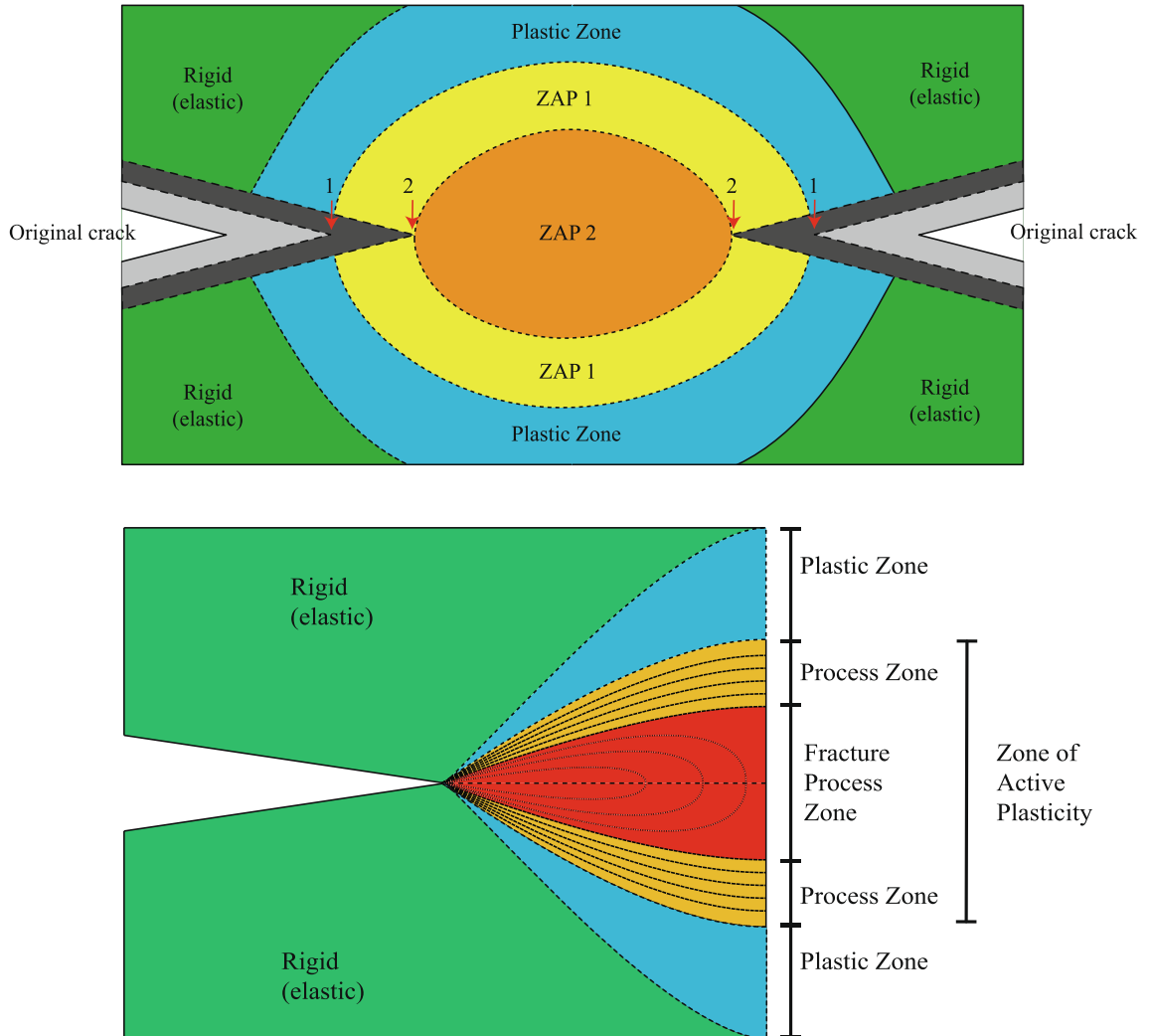


Fig. 12. Schematic of the process zones in the steady-state tearing of ultrathin, ductile sheets. The key distinction is that zones of active plasticity (ZAPs) form within a static plastic zone PZ.

plastic zone scaled with the remaining ligament. After tearing initiated, the transition to steady-state growth involved an elliptical zone of active plasticity and a transverse neck fracture process zone. The FPZ did not extend completely across the remaining ligament until very late in the steady-state crack growth regime, and the zone evolved from a trident to two-pronged fork shape that was followed by a narrow, single finger. The evolution depended on notch size because FPZ shape was influenced by interaction of the two-cracks in the DENT. Furthermore, the extent of process zones is much larger than the nominal grain size which is larger than sheet thickness. Fig. 7 shows that fracture occurred via a through thickness transverse or localized neck indicating that the asymmetry in deformation seen in Figs. 9b, 10, 11 and 13 is a bifurcation phenomenon studied extensively in the ductile materials [44–47].

We confirmed our previous assertions that the third crack growth stage was a steady-state process by comparing the height of the zone of active plasticity (denoted by the white vertical line in Fig. 13) in the transition regime to the height after steady-state was reached (Figs. 14 and 15). During the transition to steady-state growth, the initial extent of the ZAP was a function of the ligament between the starting notches. Larger remaining ligaments had larger ZAPs—the minor axis of the elliptical ZAP was 67% of the remaining ligament for the 1 mm notched specimens. Note that the very long notches (5 mm) transitioned immediately to steady-state growth. Once steady-state was reached, the ZAP was always elliptical with a minor axis extent of 45% of the remaining ligament between the crack tips. We expect that this ultrathin, ductile sheet tearing mechanism coupled with evaluation frameworks such as the one presented, will open doors to unique strategies to engineer fracture toughness.

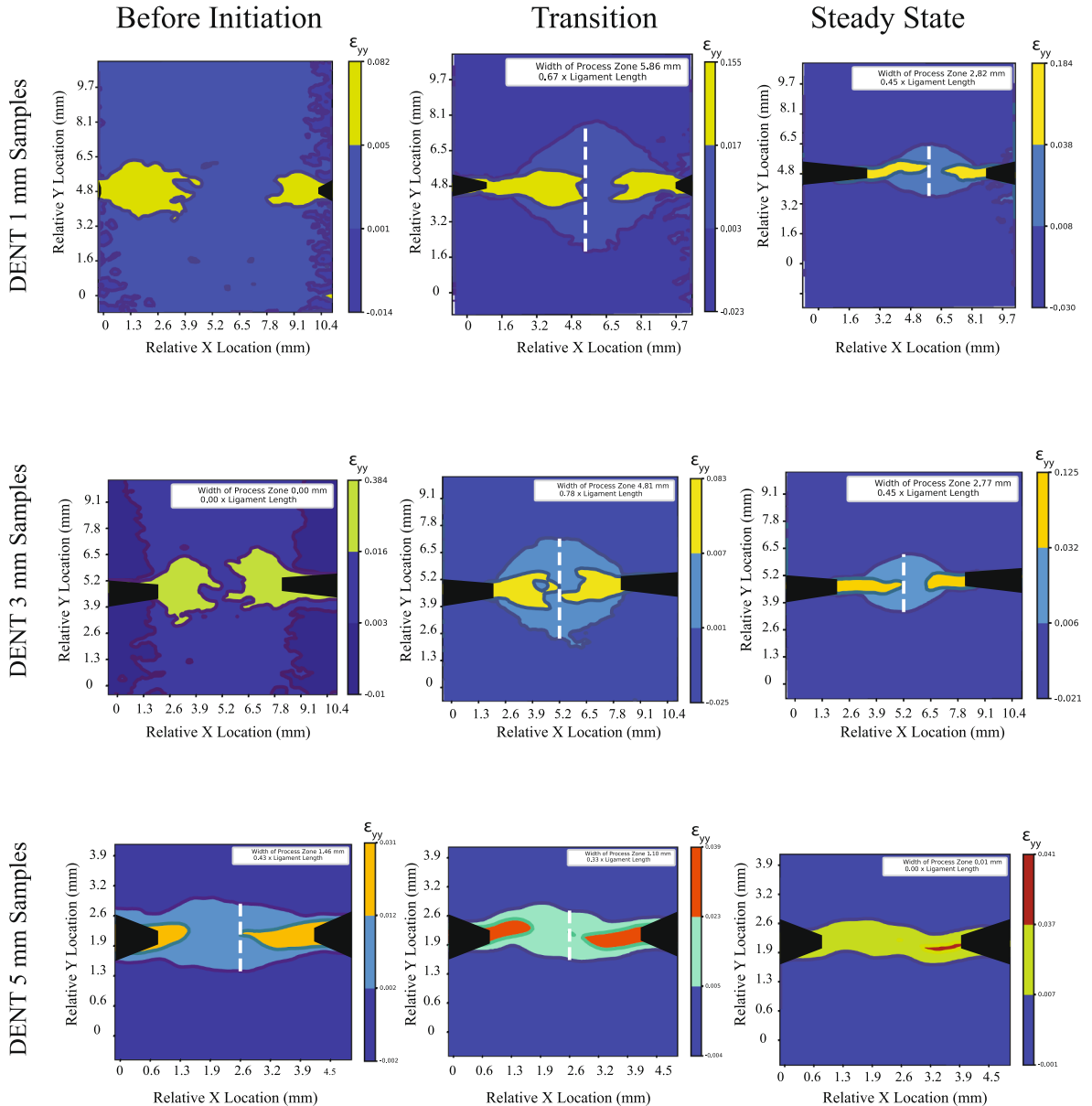


Fig. 13. Thresholded ϵ_{yy} strain maps showing the shape and size evolution of the PZ and FPZ before initiation, during the transition, and at steady-state. Cracks have been masked (black) using crack tip locations in the reference images.

4. Conclusions

Millimeter-scale, ductile sheets usually undergo a two-stage damage evolution process where fracture occurs via void nucleation and growth in a traverse neck that extends across the remaining ligament. Here we have shown that when the sheets are thinner, the mechanism changes and steady-state crack growth conditions develop. Instead of a static plastic zone developing, we showed that elliptical zones of active plasticity developed and continued to evolve after the initiation of tearing. The crack advanced through the zones of active plasticity by forming a transverse necking fracture process zone. Direct measurements of the shape and extent of the process zones were made using an incremental strain approach, and showed that an elliptical, steady-state process zone extended between the crack tips. The minor axis (height) of this zone of active plasticity progressively decreased to 45% of the remaining ligament at steady-state. The shift in tearing mechanism shows that efforts to engineer tearing resistance of ductile, ultrathin sheets will require us to understand the energetics of deformation and how the materials properties evolve in the zones of active plasticity.

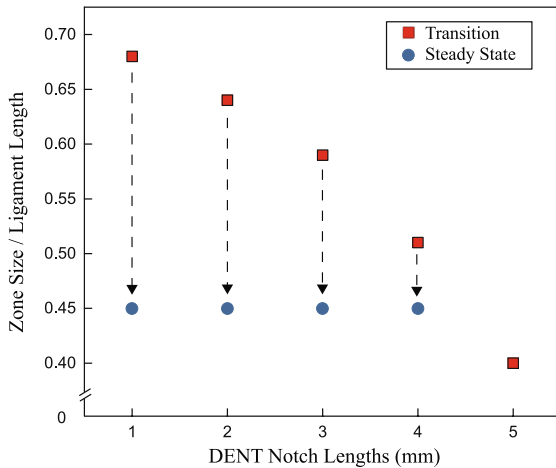


Fig. 14. Extent of the ZAPs during the transition to steady-state crack growth. The minor axis (height) of ZAPs progressively decreased from their initial values at varying notch lengths to 45% of the remaining ligament at steady-state. The extent of the steady-state zone in the strain map was defined using the thresholding scheme detailed in Fig. 10.

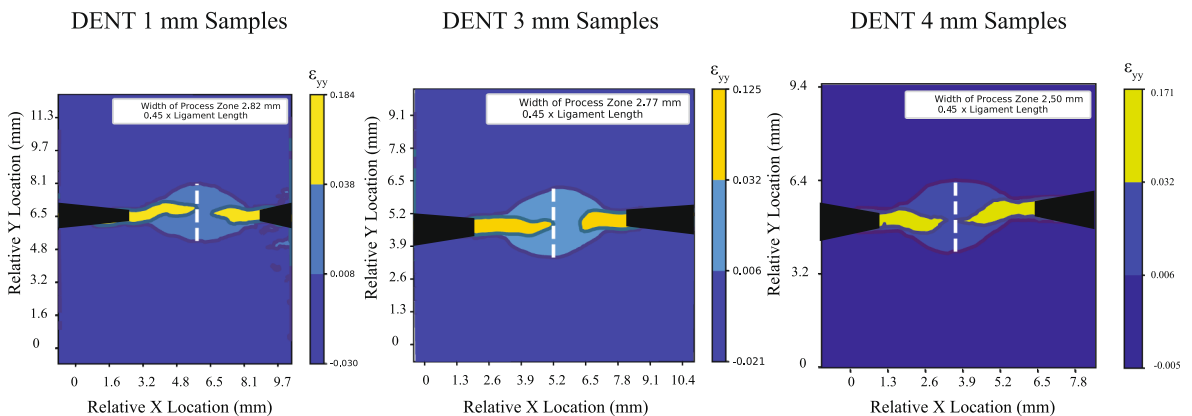


Fig. 15. Thresholded ϵ_{yy} Strain maps for DENT 1 mm; 2 mm; 4 mm samples in the steady-stage crack growth regime. The similar ZAP extents (minor axis 45% of remaining ligament) at steady-state are illustrated.

Acknowledgments

This material is based upon work supported by the National Science Foundation under Grant No. 1609817. Any opinions, findings, and conclusions or recommendations expressed in this material are those of the authors and do not necessarily reflect the views of the National Science Foundation. The authors gratefully acknowledge the additional support of the Georgia Institute of Technology.

Appendix A. ANOVA Analysis

Here we detail the general features of the algorithm and the specific open source statistics packages that were used. All of this analysis was performed using the open source Anaconda Python 2.7 (64-bit). First, we used the `optimize.curve_fit` function from the open source `numpy` Python package to fit the propagation data of the experiments to be compared to the power law given in Eq. 1.

$$\hat{\sigma} = c \times \left(1 - \left(\frac{l}{w}\right)^m\right) \quad (1)$$

The form of Eq. 1 because it represents the data well, but does not (yet) have an explicit physical meaning. Here we denote experimentally-measured stresses as σ and stress values computed from a fit as $\hat{\sigma}$. Additionally w is the specimen width, c is a fitting parameter with stress units, and m is a unitless fitting parameter. Individual, $\hat{\sigma}_i$, and ensembles of the experiments, $\hat{\sigma}_T$, were evaluated. The residuals of the least squares method linear fits were then determined.

$$\begin{aligned} r_{\ell\kappa} &= \sigma_{\ell\kappa} - \hat{\sigma}_\ell \left(\left(\frac{l}{w} \right)_{\ell\kappa} \right) \\ rI_{\ell\kappa} &= \sigma_{\ell\kappa} - \hat{\sigma}_I \left(\left(\frac{l}{w} \right)_{\ell\kappa} \right) \end{aligned} \quad (2)$$

The measured data points are given as $\sigma_{\ell\kappa}$ and $\left(\frac{l}{w} \right)_{\ell\kappa}$, which is the measurement κ taken from experiment ℓ . (Note that the subscript indices are meant to indicate individual experimental measurements of stress and crack length and simplify the ANOVA sum of squares notation. Do not confuse the indices with the similar notation of stress tensors.) The fits $\hat{\sigma}_\ell$ share the subscript of the experiment from which they were computed ℓ . The fit of all the experiments combined I is $\hat{\sigma}_I$. Thus for every data point κ from each experiment ℓ , we computed both a residual relative to individual experiment's fit $r_{\ell\kappa}$ and a residual relative to the fit of all of the combined data $rI_{\ell\kappa}$. The remainder of the analysis is a typical ANOVA of the residuals. First, the sum of squares of residuals within experiments SoSW is:

$$\begin{aligned} \text{SoSW} &= \sum_{\ell=1}^I \sum_{\kappa=1}^{K_\ell} (r_{\ell\kappa})^2 \\ df_{\text{SoSW}} &= \left(\sum_{\ell=1}^I K_\ell \right) - I = n - I \end{aligned} \quad (3)$$

The summation encompasses the total number of experiments I we compared and the total number of measurements within each individual experiment K_ℓ . The degrees of freedom for SoSW is df_{SoSW} , which incorporates the grand total n of measurements from all of the experiments combined I . Rather than directly computing the sum of squares of residuals between experiments, we computed the total sum of squares of residuals SoST.

$$\text{SoST} = \sum_{\ell=1}^I \sum_{\kappa=1}^{K_\ell} (rI_{\ell\kappa})^2 \quad (4)$$

And then computed the desired sum of squares of residuals between experiments SoSB.

$$\begin{aligned} \text{SoST} &= \text{SoSW} + \text{SoSB} \\ \text{SoSB} &= \text{SoST} - \text{SoSW} \\ df_{\text{SoSB}} &= I - 1 \end{aligned} \quad (5)$$

The final step of the ANOVA is computation of the mean sums of squares and a F value computation, which in conjunction with the degrees of freedom of the respective sums of squares (df_{SoSW} and df_{SoSB}) was used to compute p -values using the open source SciPy "stats" module: `scipy.stats.f.sf(F, dfSoSW, dfSoSB)`.

$$F = \frac{\text{SoSB}/df_{\text{SoSB}}}{\text{SoSW}/df_{\text{SoSW}}} \quad (6)$$

We iteratively removed the shortest normalized crack length datapoint $(\left(\frac{l}{w} \right)_{\ell\kappa}, \sigma_{\ell\kappa})$ from consideration, then the next shortest normalized crack length data point was excluded, and so on while re-calculating the entire ANOVA of residuals getting a new F test and p -value each time. Once the p -value exceeded a confidence level of 0.01, we considered the data to have converged and steady-state conditions established. The data points from the onset of steady-state through the end of the experiment were then fit with a linear least square fit (again using Python), and the intercept at a normalized crack length of zero was σ_c .

Appendix B. Supplementary material

Supplementary data associated with this article can be found, in the online version, at <https://doi.org/10.1016/j.engfracmech.2019.106540>.

References

- [1] Hahn GT, Rosenfield AR. Local yielding and extension of a crack under plane stress. *Acta Metall* 1965;13(3):293–306. [https://doi.org/10.1016/0001-6160\(65\)90206-3](https://doi.org/10.1016/0001-6160(65)90206-3).
- [2] Kang K-J, Beom HG. Plastic zone size near the crack tip in a constrained ductile layer under mixed mode loading. *Eng Fract Mech* 2000;66(3):257–68. [https://doi.org/10.1016/S0013-7944\(00\)00023-0](https://doi.org/10.1016/S0013-7944(00)00023-0).
- [3] Banks T, Garlick A. The form of crack tip plastic zones. *Eng Fract Mech* 1984;19(3):571–81. [https://doi.org/10.1016/0013-7944\(84\)90012-2](https://doi.org/10.1016/0013-7944(84)90012-2).
- [4] Cotterell B, Atkins A. A review of the J and I integrals and their implications for crack growth resistance and toughness in ductile fracture. *Int J Fract* 1996;81(4):357–72. <https://doi.org/10.1007/BF00012428>.
- [5] Zhu XK, Joyce JA. Review of fracture toughness (G, K, J, CTOD, CTOA) testing and standardization. *Eng Fract Mech* 2012;85:1–46. <https://doi.org/10.1016/j.engfracmech.2012.02.001>.
- [6] Anderson TL. Fracture mechanics: fundamentals and applications. 4th ed. Boca Raton: CRC Taylor and Francis; 2017. dT BOOK xvi, 688 p.: ill.; 26 cm.
- [7] Broek D. Elementary engineering fracture mechanics. 4th ed. Boston: Martinus Nijhoff; Distributed by Kluwer, Dordrecht; 1986. dT BOOK xiv, 501

- p.: ill.; 23 cm.
- [8] Rice JR, Rosengren GF. Plane strain deformation near crack tip in power-law hardening material. *J Mech Phys Solids* 1968;16(1):1–12.
 - [9] Moran B, Shih CF. Crack tip and associated domain integrals from momentum and energy-balance. *Eng Fract Mech* 1987;27(6):615–42.
 - [10] Hutchinson JW. Singular behaviour at the end of a tensile crack in a hardening material. *J Mech Phys Solids* 1968;16(1):13–31.
 - [11] Rice JR, Rosengren GF. Plane strain deformation near a crack tip. *J Mech Phys Solids* 1968:1–12.
 - [12] Rice JR. A path independent integral and approximate analysis of strain concentration by notches and cracks. *J Appl Mech* 1968;35(2):379.
 - [13] Lanning W, Javaid S, Muhlstein C. Reconciling fracture toughness parameter contradictions in thin ductile metal sheets. *Fatigue Fract Eng Mater Struct* 2017;1–16. <https://doi.org/10.1111/ffe.12600>.
 - [14] McMeeking R, Parks D. On criteria for J-Dominance of crack-tip fields in large-scale yielding. Landes J, Begley J, Clarke G, editors. *Elastic-plastic fracture*, Vol. STP668. ASTM; 1979. p. 175–94.
 - [15] Xia L, Shih CF, Hutchinson JW. A computational approach to ductile crack-growth under large-scale yielding conditions. *J Mech Phys Solids* 1995;43(3):389–413.
 - [16] Amazigo J, Hutchinson J. Crack-tip fields in steady crack-growth with linear strain-hardening. *J Mech Phys Solids* 1977;25(2):81–97. [https://doi.org/10.1016/0022-5096\(77\)90005-9](https://doi.org/10.1016/0022-5096(77)90005-9) <<https://www.sciencedirect.com/science/article/pii/0022509677900059>>.
 - [17] Pineau A, Benzerga AA, Pardoen T. Failure of metals I: brittle and ductile fracture. *Acta Mater* 2016;107:424–83. <https://doi.org/10.1016/j.actamat.2015.12.034>.
 - [18] Clutton E. Essential work of fracture. *Eur Struct Integrity Soc* 2001;28(C):177–95. [https://doi.org/10.1016/S1566-1369\(01\)80033-9](https://doi.org/10.1016/S1566-1369(01)80033-9).
 - [19] Mai YW, Cotterell B. The essential work of fracture for tearing of ductile metals. *Int J Fract* 1984;24(3):229–36. <https://doi.org/10.1007/BF00032685>.
 - [20] Mai YW, Cotterell B. Effect of specimen geometry on the essential work of plane stress ductile fracture. *Eng Fract Mech* 1985;21(1):123–8. [https://doi.org/10.1016/0013-7944\(85\)90059-1](https://doi.org/10.1016/0013-7944(85)90059-1).
 - [21] Pardoen T, Marchal Y, Delannay F. Essential work of fracture compared to fracture mechanics-towards a thickness independent plane stress toughness. *Eng Fract Mech* 2002;69(5):617–31. [https://doi.org/10.1016/S0013-7944\(01\)00099-6](https://doi.org/10.1016/S0013-7944(01)00099-6).
 - [22] Pardoen T, Hachez F, Marchionni B, Blyth PH, Atkins AG. Mode I fracture of sheet metal. *J Mech Phys Solids* 2004;52(2):423–52. [https://doi.org/10.1016/S0022-5096\(03\)00087-5](https://doi.org/10.1016/S0022-5096(03)00087-5).
 - [23] Cotterell B, Reddel JK. The essential work of plane stress ductile fracture. *Int J Fract* 1977;13(3):267–77.
 - [24] Cotterell B, Pardoen T, Atkins AG. Measuring toughness and the cohesive stress-displacement relationship by the essential work of fracture concept. *Eng Fract Mech* 2005;72(6 SPEC. ISS.):827–48. <https://doi.org/10.1016/j.engfracmech.2004.10.002>.
 - [25] Banerjee S. Influence of specimen size and configuration on the plastic zone size, toughness and crack growth. *Eng Fract Mech* 1981;15(3–4):343–90. [https://doi.org/10.1016/0013-7944\(81\)90065-5](https://doi.org/10.1016/0013-7944(81)90065-5).
 - [26] Saxena A. *Nonlinear fracture mechanics for engineers*. 2nd ed. CRC Press; 1998.
 - [27] Lanning WR, Johnson C, Javaid S, Muhlstein C. Mode I steady-state crack propagation through a fully-yielded ligament in thin ductile metal foils. *Theoret Appl Fract Mech* doi:<https://doi.org/10.1016/j.tafmec.2018.12.006>.
 - [28] Anderson TL. *Fracture mechanics: fundamentals and applications*. CRC Press; 2017.
 - [29] ASTM International, ASTM E345–16 Standard Test Methods of Tension Testing of Metallic Foil.
 - [30] Properties of Wrought Aluminum and Aluminum Alloys; 1990.
 - [31] Hordon MJ, Lement BS, Averbach BL. Influence of plastic deformation on expansivity and elastic modulus of aluminum. *Acta Metall* 1958;6(6):446–53. [https://doi.org/10.1016/0001-6160\(58\)90023-3](https://doi.org/10.1016/0001-6160(58)90023-3).
 - [32] Rosenmayer CT, Brotzen FR, Gale RJ. Mechanical testing of thin films. *MRS Proc* 1988;130:77. <https://doi.org/10.1557/PROC-130-77>.
 - [33] Hoffman RW. Nanomechanics of thin films: emphasis: tensile properties. *MRS Proc* 1988;130:295. <https://doi.org/10.1557/PROC-130-295>.
 - [34] Heinen D, Bohn HG, Schilling W. On the mechanical strength of freestanding and substrate-bonded al thin-films. *J Appl Phys* 1995;77(8):3742–5. <https://doi.org/10.1063/1.360279>.
 - [35] Heinen D, Bohn HG, Schilling W. Internal-friction in freestanding thin al films. *J Appl Phys* 1995;78(2):893–6. <https://doi.org/10.1063/1.358546>.
 - [36] Hinai M, Sawaya S, Masumoto H. Effect of cold-working on mechanical damping capacity of al-co alloys. *Mater Trans* 1993;34(4):359–63. <https://doi.org/10.2320/matertrans.M2012418>.
 - [37] Read DT, Cheng Y-W, Keller RR, McColskey JD. Tensile properties of free-standing aluminum thin films. *Scripta Mater* 2001;45(5):583–9. [https://doi.org/10.1016/S1359-6462\(01\)01067-3](https://doi.org/10.1016/S1359-6462(01)01067-3).
 - [38] Li XC, Yang YY, Wang YZ, Bao J, Li SP. Effect of the material-hardening mode on the springback simulation accuracy of v-free bending. *J Mater Process Technol* 2002;123(2):209–11.
 - [39] Li QD, Hua GM, Lu H, Yu B, Li DY. Understanding the effect of plastic deformation on elastic modulus of metals based on a percolation model with electron work function. *JOM* 2018;70(7):1130–5. <https://doi.org/10.1007/s1183>.
 - [40] Mott NF. A theory of work-hardening of metal crystals. *Phil Mag* 1952;43(346):1151–78. <https://doi.org/10.1080/14786441108521024>.
 - [41] Friedel J. Anomaly in the rigidity modulus of copper alloys for small concentrations. *Phil Mag* 1953;44(351):444–8. <https://doi.org/10.1080/14786440408520327>.
 - [42] Blanter MS, Golovin IS, Neuhauser H, Sinnning HR. *Internal friction in metallic materials: a handbook*. Springer series in materials science vol. 90. Berlin, Berlin: Springer-Verlag; 2007. pp. 537. doi:[10.1007/978-3-540-68758-0](https://doi.org/10.1007/978-3-540-68758-0).
 - [43] ASTM, B871 Standard Test Method for Tear Testing of Aluminum Alloy Products, Annual Book of ASTM Standards, ASTM, West Conshohocken, PA; 2013.
 - [44] Stören S, Rice J. Localized necking in thin sheets. *J Mech Phys Solids* 1975;23(6):421–41.
 - [45] Zhang R, Shao Z, Lin J. A review on modelling techniques for formability prediction of sheet metal forming. *Int J Lightweight Mater Manuf* 2018;1(3):115–25.
 - [46] Hill R, Hutchinson JW. Bifurcation phenomena in the plane tension test. *J Mech Phys Solids* 1975;23(4–5):239–64. [https://doi.org/10.1016/0022-5096\(75\)90027-7](https://doi.org/10.1016/0022-5096(75)90027-7).
 - [47] Audoly B, Hutchinson JW. Analysis of necking based on a one-dimensional model. *J Mech Phys Solids* 2016;97:68–91.